Modular solar-to-fuels electrolysis at low cell potentials enabled by glycerol electrooxidation and a bipolar membrane separator

Hamed Mehrabi[1], Zebulon G. Schichtl[2], Samuel K. Conlin[2], Robert H. Coridan[1,2*]

[1] Materials Science and Engineering Program, University of Arkansas, Fayetteville, AR, 72701, USA.

[2] Department of Chemistry and Biochemistry, University of Arkansas, Fayetteville, AR, 72701, USA

* rcoridan@uark.edu

Abstract

Solar fuel generation through water electrolysis or electrochemical CO_2 reduction is thermodynamically limited when paired with the oxygen evolution reaction (OER). The glycerol electrooxidation reaction (GEOR) is an alternative anodic reaction with lower anodic electrochemical potential that utilizes a renewable coproduct produced during biodiesel synthesis. We show that GEOR on a Au-Pt-Bi ternary metal electrocatalyst in a model alkaline crude glycerol solution can provide significant cell potential reductions even when paired to reduction reactions in seawater and acidic catholytes via a bipolar membrane (BPM). We showed that the combination of GEOR electrooxidation and a BPM separator lowers the total cell potential by 1 V at an electrolysis current of 10.0 mA cm^{-2} versus to an anode performing OER when paired with hydrogen evolution and CO_2 reduction cathodes. The observed voltage reduction was steady for periods of up to 80 hours, with minimal glycerol crossover observed through the membrane. These results motivate new, high-performance cell designs for photoelectrochemical solar fuels integrated systems based on glycerol electrooxidation.

Keywords: solar-to-hydrogen, glycerol electrooxidation, alternative oxidation reactions, electrocatalysis, bipolar membranes

Table of Contents Figure

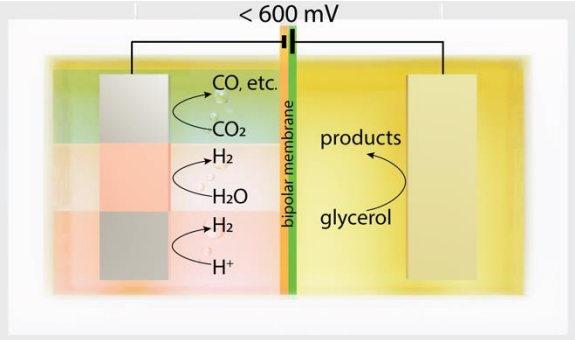

Introduction

Technological advances have increased the competitiveness of solar-generated electricity compared to electricity generated from fossil fuels. Similar advances are necessary to improve the direct conversion of sunlight to fuels as a storage medium.[1–3] Important solar fuels reactions include water electrolysis (solar-to-hydrogen, STH) or electrocatalytic CO_2 reduction to produce useful products such as methanol or ethanol.[4–9] A fundamental limit to the energy storage efficiency of these processes is the choice of reaction on the anode. In water, the anodic reaction is generally water oxidation, where the cathodic products are kept and the O_2 is discarded. The water oxidation potential (E^0 = 1.23 V vs. RHE at 25 °C, Equations S1-S4) and associated kinetic overpotentials limit the achievable energy conversion efficiencies for the products of interest that are produced at the cathode.[10–13] The glycerol electrooxidation reaction (GEOR) is an appealing alternative to water oxidation at the anode for pairing with fuel-forming reactions at the cathode.[14–17] Glycerol is a coproduct of the transesterification reaction that produces biodiesel.[18–20] Roughly 3 million tons of glycerol was produced in 2020 from biodiesel manufacturing, higher than its global demand.[21] As a result, there is significant scientific and engineering interest in adding value to the abundant glycerol supply by chemical transformation.

Glycerol is well-understood as a sacrificial electrooxidation substrate for replacing water oxidation in anodic reactions. GEOR occurs at lower positive potentials on the anode than for water oxidation in both acidic or basic electrolytes and results in a variety of products such as glyceraldehyde, dihydroxyacetone, and a variety of organic acids.[22–26] It has been shown that a mixed metal electrocatalyst composed of Au, Pt, and Bi is capable of achieving cell potentials of less than 600 mV for sustained GEOR-assisted hydrogen evolution in a model crude glycerol solution. The low cell potentials are attributed to the reaction being limited to the two-electron oxidation of glycerol to dihydroxyacetone or glyceraldehyde. Based on Gibbs free energies of formation, the thermodynamic oxidation potentials for glycerol to dihydroxyacetone or to glyceraldehyde were estimated to be 0.05 V and 0.19 V vs. RHE, respectively.[27] More positive anode potentials, and hence higher overall cell potentials, were required to oxidize either glyceraldehyde or dihydroxyacetone further. Hydrogen was separated from the anode by a ceramic anion exchange membrane, which constrained the HER electrocatalysis to the same alkaline electrolyte conditions as in the anolyte. This is not necessarily an ideal electrochemical environment for hydrogen evolution. More generally, it limits the practicality of the GEOR-derived cell voltage saving combination with other fuel-forming cathodic reactions such as

seawater electrolysis, CO_2 reduction, or photoelectrochemical (PEC) devices driving these reactions. Bipolar membranes (BPMs) are layered structures composed of an anion exchange and a cation (or proton) exchange layer.[28–30] Water dissociation between these layers, either natural or catalyzed by metal oxide particles, provides hydronium to the catholyte and hydroxide to the anolyte, respectively.[31–33] This effectively enables optimized, yet disparate electrolytic half-reactions to communicate electrochemically.

Here, we characterize the use of a commercial BPM for separating the anodic oxidation of a model crude glycerol solution from a generalizable, fuel-forming reduction reaction in an independent catholyte. BPMs have been used to separate disparate environments for water electrolysis half-cells.[34–36] We show that a BPM can also be used for separating the GEOR electrolyte from a variety of critical fuel-forming reactions, including the hydrogen evolution reaction (HER) in acid, HER in model seawater, and for CO_2RR in a bicarbonate buffer. In every case tested, the overall cell potential was reduced by roughly 1V compared to the same cathode paired with an OER anode. We show that the operating point of these systems can be predicted from a load-line analysis of independent three-electrode measurements when the turn-on potential drop across the BPM is considered in the series load. This allows for the coordination of optimized half-cell reactions for the overall design of GEOR-assisted electrolysis and photoelectrochemical systems. Finally, we show that the combination of a GEOR anode and BPM separator can sustain the nearly 1V reduction in cell potentials for extended periods (>20 hours) in quiescent solutions with minimal glycerol crossover.

Materials and Methods

Acetone (HPLC grade; VWR), methanol (HPLC grade; VWR), isopropyl alcohol (HPLC grade; VWR), and water (HPLC grade; BDH) were used as received. Ultra-high purity nitrogen (99.999%; Airgas) was used to dry electrode materials. Hydrochloric acid (HCl, 1 N; VWR) was used as received for removing native oxides from the Ni foam surface. Sodium hydroxide (NaOH, 50% w/w; Sigma-Aldrich), glycerol ($C_3H_8O_3$, USP grade; Bluewater Chemgroup), sulfuric acid (H_2SO_4, 98%; Sigma-Aldrich), sodium carbonate decahydrate (99.95%; Sigma-Aldrich), and artificial sea salt mix (ASTM D1141-98; Lake Products Company) were used for the HER, OER, and CO_2RR electrolytes as described in the text. Sodium tetrachloroaurate(III) dihydrate ($NaAuCl_4 \cdot 2H_2O$, 99%; Sigma Aldrich), potassium tetrachloroplatinate(II) (K_2PtCl_4, 98%, Sigma-Aldrich), and bismuth(III) nitrate pentahydrate ($Bi(NO_3)_3 \cdot 5\ H_2O$, 99.99%; Sigma-Aldrich) were used to synthesize electrocatalysts layers on Ni foam electrodes. A Ag/AgCl

reference electrode (saturated KCl; BASi) was used for all electrochemical experiments. Commercial anion exchange membrane (Selemion AMVN; AGC Group) and bipolar membrane (Fumasep FBM-PK; Fumatech) sheets were used to separate the anode and cathode compartments as described. A potentiostat (Biologic SP-240) was used for electrochemical analysis. In supplemental experiments, anolyte was circulated using a peristaltic pump (New Era Pump Systems NE-9000) where circulation is noted. The recycled anolyte flow was directed directly at the porous anode at 30 ml min^{-1} for the duration of the electrocatalysis.

Electrode preparation

Nickel foam (99.99%; MTI) electrodes were prepared from 10×15 mm rectangle flags. The electrode flags were mechanically connected to a Ni bus wire via a crimping barrel. The bus wire was passed through a glass tube, then the pressed section of the foam, wires, and glass tube end was sealed using a chemically stable two-part epoxy adhesive (Loctite 9460) and cured for at least 24 hours prior to use. The geometric area of each nickel foam electrode was 1 cm^2. GEOR electrocatalysts were fabricated on Ni foam electrodes as described in previous work.[27] The foam was first rinsed with acetone, methanol, isopropyl alcohol, and water in sequence, then dried using a stream of nitrogen. This was done to remove any possible organic residue from the surface of the electrode. The electrodes were then placed in a 1 N HCl solution for 10 minutes to remove the native nickel oxide layer. After rinsing with water, gold and platinum were deposited in sequence on the clean nickel foam electrode by the galvanic replacement reaction. First, the nickel foam was placed in a gold deposition solution (0.4 mM $NaAuCl_4$ in 10.0 mM H_2SO_4) for 5 minutes, then rinsed with water, then placed in a platinum deposition solution (0.6 mM K_2PtCl_4 in 10.0 mM H_2SO_4) for 5 minutes. The Au-Pt-coated electrode was then rinsed with water and placed in an electrochemical cell containing a 1.0 mM $Bi(NO_3)_3$ in 1.0 M nitric acid solution, a graphite rod as a counter electrode, and a Ag/AgCl reference electrode. A layer of bismuth was electrodeposited onto the Au-Pt-coated Ni foam electrode at -15.0 mA cm^{-2} for 5 seconds, producing an Au-Pt-Bi-coated Ni electrode for the GEOR electrocatalysis. Detailed analysis of the structure and chemical composition and analysis of the Au-Pt-Bi-coated Ni electrodes can be found elsewhere.[27] Pt-coated Ni foam electrodes used for HER and OER were fabricated by placing the rinsed and dried Ni foam electrodes in a 0.6 mM K_2PtCl_4 solution for 10 minutes. Au-coated Ni foam electrodes used for CO_2RR were fabricated by placing the rinsed and dried Ni foam electrodes in a 0.4 mM $NaAuCl_4$ solution for 10 minutes.

The model crude glycerol electrooxidation reaction solution consisted of a 2.0 M NaOH solution in a 1:4 w/w ratio of glycerol and water. A 2.0 M NaOH solution was used for comparative oxygen evolution reaction (OER) anolyte. A 2.0 M H_2SO_4 solution was prepared for use as an acidic HER catholyte. A model seawater catholyte was prepared by mixing 41.9 g L^{-1} of the artificial sea salt mix with HPLC water. CO_2RR was performed in a 0.500 M Na_2CO_3 solution. Na_2CO_3 was chosen (rather than $NaHCO_3$, for example) because it could be obtained at a higher purity. Equilibration with bubbling CO_2 resulted in the same buffer composition. For CO_2 reduction, the Na_2CO_3 solution was purged with CO_2 at 7 sccm with the gas bubbling directly against the Au-coated Ni electrode. The headspace products were characterized using an SRI 6810-C gas chromatograph (GC) inline to the output stream of the cell. The GC was equipped with a 2 m Haysep-D column, a flame ionization detector (FID), and a thermal conductivity detector (TCD) for CO_2 product detection. The glycerol oxidation products and molecular crossover were characterized using a Bruker 500 nuclear magnetic resonance (NMR) spectrometer. FEI Nova Nanolab scanning electron microscope (SEM) equipped with energy-dispersive X-ray spectroscopy (EDX) was used to analyze the elemental composition of deposition from the solution on the Pt-coated Ni foam cathode during seawater electrolysis. EDX was also used characterize the composition of foam electrodes before and after electrolysis to verify the presence of the electrocatalyst layer after extended electrolysis. A 3D schematic of the electrochemical cell is shown in Figure S1.

Load Line Analysis (LLA) procedure for three-electrode measurements

The properties of a two-electrode system can be predicted by analyzing the three-electrode IR-compensated cyclic voltammetry versus a common reference electrode of each half-cell with the other. In a two-electrode electrochemical cell, the current passed through the anode and cathode are equal. The operating potential of the electrochemical cell in this configuration is the potential at which the current passed through the anode matches that of the cathode.[37] If the anode and cathode areas are the same, it is equivalent to match the current densities to find an operating current density, j_{op}. The graphical representation of this procedure is shown in Figure 1. The required applied potential (V_{op}) can be determined for a given operational current (I_{op}) using a LLA procedure. The potential predictions of a LLA account for the potentials of each electrochemical reaction, disregarding any potential requirements from other elements of the electrochemical system. A bipolar membrane has a corresponding turn-on bias which needs to be accounted for in a LLA. In addition, the load-line analysis is based on sweeping voltametric

measurements, which are dynamic methods to study the system and long-term effects, such as ion depletion close to the catalyst surface and the resulting concentration polarization. LLA does not account for the solution and BPM electrochemical resistance or the non-faradic potential losses unless they are included in the effective circuit of analysis. A more accurate prediction of the operating point would include these details, though they are sensitive to the details of a specific cell assembly, including the relative electrode placement, orientation, and membrane size. The benefit of a LLA is to approximate what operating characteristics are achievable for a cell based on an anode and cathode pair with the measured electrocatalytic properties. Hence, it provides an upper bound on the performance in the absence of further limitations that can be ascribed to the design of a particular system construction.

The turn-on bias, V_{BPM}, required to drive current through the BPM can be understood from calculating the cell potential required to drive the ionization of water molecules. The autoionization equilibrium constant for water at 25 ºC is $K_W = 1.0 \times 10^{-14}$. Hence, the reaction is not spontaneous at the conditions of interest in this work. The standard Gibbs free energy for this reaction is:

$$\Delta G = - RT \ln K_W = 79.9 \text{ kJ mol}^{-1}.$$

This corresponds to a cell potential of:

$$V_{BPM} = -\Delta G/(n F) = -0.83 \text{ V},$$

where n = 1, the number of electrons total required per molecule of water dissociation, and F is Faraday's constant. This can be understood as an electrochemical cell by coupling Equation S1 as the cathode reaction occurring at the cation exchange layer of the BPM and Equation S3 as the anode reaction at the anion exchange layer. These are roughly the electrolyte conditions within the corresponding layers of the BPM itself.

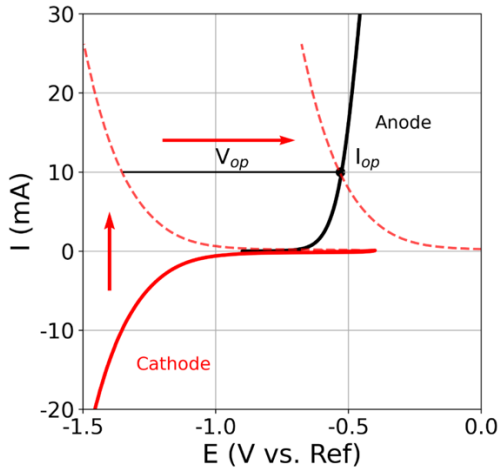

Figure 1 - Load-line analysis of anodic and cathodic reactions, the theoretical cell potential at a given current passed corresponds to the shift required for the reactions to cross at that current. The operational current and applied potential are represented as I_{op} and V_{op}, respectively.

Electrochemical characterization

The electrochemical cell was set up for each anodic and cathodic environment with the BPM oriented in reverse bias (cation exchange layer on the cathode side). IR-compensated, three-electrode CV measurements were performed on each half-cell reaction, with the Ag/AgCl reference electrode was placed in the working electrode cell. A summary list of the relevant reactions is provided in Table S1. The data gathered from the CV measurements were used to predict two-electrode cell potential for each reaction pair using a LLA. Two electrode chronopotentiometry (CP) experiments were performed at a cathode current density (*j*) of –10.0 mA cm^{-2} for the noted extended periods to compare actual cell potential vs. LLA prediction. This current density was chosen as representative of rates targeted for photoelectrochemical solar-to-hydrogen systems.[38] The two-electrode CP experiments were performed for hydrogen generation in acid (denoted as aHER), and in seawater (sHER), paired with OER and GEOR in alkaline conditions with the anode and cathode compartments separated by a BPM. The CO_2 reduction reaction in a CO_2-purged sodium bicarbonate catholyte was paired with GEOR using a BPM, and with OER in a sodium bicarbonate solution (bOER) separated by a Selemion membrane. These experiments were chosen to compare the conventional CO_2RR conditions with the GEOR-BPM combination.

Crossover of compounds between chambers may affect the reaction efficiency and electrocatalyst lifetime. Glycerol crossover through the BPM was studied to determine the magnitude and rate of permeation over several days. For these experiments, CO_2RR in 25 ml of 0.500 M Na_2CO_3 solution prepared in D_2O was paired with GEOR at 10.0 mA cm^{-2} for 24 hours

in a two-electrode configuration. 400 µL aliquots of the catholyte were sampled at 6, 18, and 24 hours during the electrolysis. The solutions remained in the cell without electrolysis for 48 hours after the end of the CP experiment and were sampled at 48 and 72 hours after the start of the experiment. The concentration of glycerol in the Na_2CO_3 solution was determined using ^1H NMR with a DMSO internal standard for quantification.

Results and Discussion

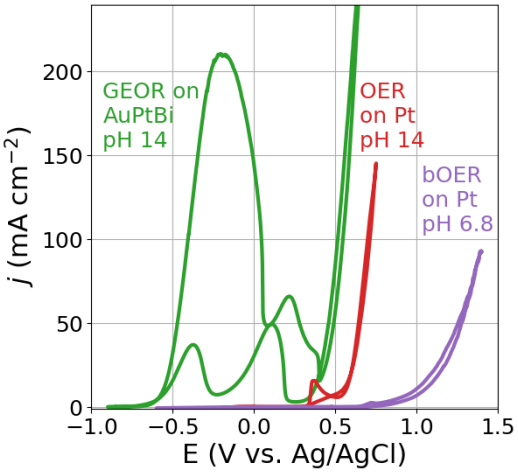

Figure 2 - Cyclic voltammetry of the GEOR (glycerol electrooxidation reaction in 2.0 M NaOH + 20% glycerol) on Au-Pt-Bi-coated Ni foam electrocatalyst in green compared to OER (oxygen evolution reaction in 2.0 M NaOH) on Pt-coated Ni foam in red and bOER (oxygen evolution reaction in a CO_2 saturated 0.500 M Na_2CO_3 buffered solution) in purple vs. Ag/AgCl reference electrode.

We compared the electrochemical current density-electrode potential (*j-E)* characteristics of the relevant anodic half-reactions as measured by cyclic voltammetry (CV). The three-electrode CV measurements of the anodic reactions under comparison, (OER and GEOR), are shown in Figure 2. OER on a Pt-coated Ni electrode shows an onset of 10.0 mA cm^{-2} at 0.56 V vs. Ag/AgCl at pH 14 and 1.05 V vs. Ag/AgCl in the sodium bicarbonate solution at pH 6.8. The onset potential difference in these solutions can be explained by the Nernstian potential shift of the oxygen reduction potential due to pH difference.[39] The GEOR CV shows two oxidation waves with onsets of -0.56 V vs. Ag/AgCl and 0.36 V vs. Ag/AgCl. These correspond to glycerol electrooxidation on the metallic electrocatalyst surface and the oxidized electrocatalyst surfaces, respectively.[16] Both of these potentials are less positive than that of OER at high pH values. The oxidized electrocatalyst surface is likely very stable at high current densities as well. However, it is only 0.2 V negative of the OER potential. This would limit the cell potential advantages for using GEOR paired with an HER cathode compared to the overall water splitting reaction. The metallic GEOR electrocatalyst can save up to 1.0 V by a similar comparison.

We used similar *j-E* characteristic measurements of cathode/catholyte half-cells from three electrode CV measurements to characterize full electrolysis cells using a BPM separator. Measuring *j-E* characteristics for each of the half-cell reactions with respect to the same reference (here, an Ag/AgCl reference electrode) enabled a standard LLA for predicting two-electrode operation. The operating cell voltage can be found for a given pair of anode and cathode half-reactions from the difference between the absolute potentials of the anode and cathode at a matched current when taking the electrode areas into account.[37] Here, electrodes with 1 cm^2 geometric areas were used in each experiment, so it is equivalent to match the current densities on the anode and cathode. A LLA including a BPM requires the addition of the rectifier voltage drop, V_{BPM} = -0.83 V, to initiate current through the membrane.[36,40–44] Therefore, the predicted operating cell voltage (V_{op}) for a current density of –10.0 mA cm^{-2} through the cathode can be predicted from the half-cell potentials of the cathode (E_{cat}) at -10.0 mA cm^{-2}, and anode (E_{an}) at +10.0 mA cm^{-2}, respectively: $V_{op} = E_{cath} - E_{an} + V_{BPM} = \Delta E + V_{BPM}$. The operating potential is defined with convention that $V_{op} < 0$ V indicates that the pairing forms an electrolytic cell.

The three-electrode *j-E* measurement for HER on a Pt-coated Ni mesh HER cathode measured in 1 M H_2SO_4 is shown in Figure 3a, along with the *j-E* measurements for the GEOR and OER electrocatalysts in 2 M NaOH (with 20% (w/w) glycerol for GEOR). For combining the HER cathode in the acidic electrolyte (aHER) and the OER anode in a single cell, the difference in electrode potentials (ΔE) at -10.0 mA cm^{-2} is -0.78 V. A similar comparison of the aHER cathode and the GEOR anode results in ΔE= 0.28V, which incorrectly suggests that the reaction is spontaneous. However, accounting for V_{BPM} in both LLA resulted in predictions of negative, electrolytic cell potentials for both cells. The predicted operating cell potentials are V_{op} = -1.61 V for the aHER|BPM|OER cell and V_{op} = -0.55 V for the aHER|BPM|GEOR cell.

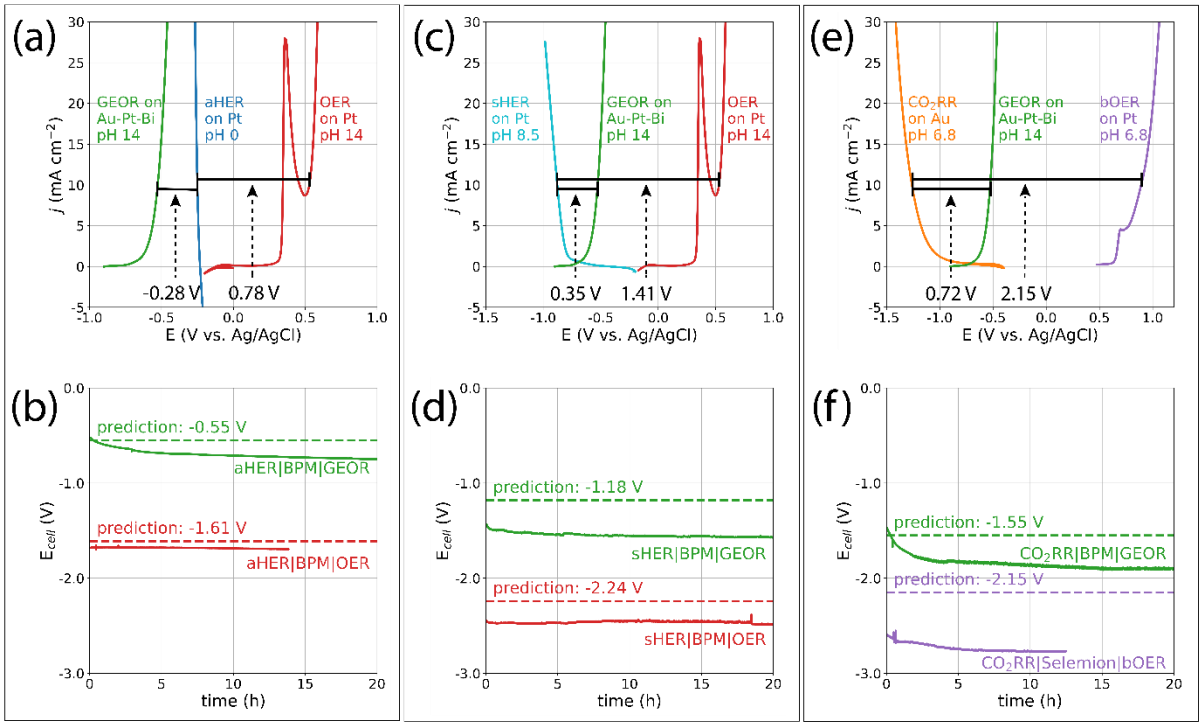

Figure 3: (a) Load-line analysis of HER in 2.0 M H_2SO_4 paired with GEOR and OER at pH 14. (b) Chronopotentiometry at -10.0 mA cm^{-2} of the aHER|BPM|GEOR (green) and aHER|BPM|OER (red) electrochemical cells. (c) LLA of HER in sea water paired with GEOR and OER at pH 14. (d) Chronopotentiometry at -10.0 mA cm^{-2} of the sHER|BPM|GEOR (green) and sHER|BPM|OER (red) electrochemcial cells. (e) LLA of CO_2RR in 0.5 M Na_2CO_3 paired with GEOR and bOER. (f) Chronopotentiometry of CO_2RR|BPM|GEOR (green) and CO_2RR|Selemion|bOER (purple) at -10.0 mA cm^{-2}.

Measurements of the cell potential in two-electrode chronopotentiometry (CP) experiments at a cathodic current density of -10.0 mA cm^{-2} (Figure 3b) showed slightly higher cell potentials for both pairs of reactions. The aHER|BPM|OER cell operated at a cell potential of -1.65 V, which increased to -1.69 V by the end of the 13 hr experiment. The difference is likely due to solution and membrane resistances not accounted for in the load-line analysis and otherwise not characterized here. The aHER|BPM|GEOR cell began at roughly the predicted operating potential of -0.52 V, then monotonically increased in magnitude to -0.74 V after 20 hours. The increase in cell potential over time was observed previously and attributed to the slow formation of Pt hydroxides on the surface of the Au-Pt-Bi anode. Regardless, pairing the Pt HER cathode in 2 M H_2SO_4 with the GEOR anode reduced the cell potential by roughly the 1 V predicted by the LLA compared to water electrolysis.

Seawater electrolysis is also a significant reaction for H_2 evolution. Seawater is an important potential feedstock due to its widespread accessibility.[45] A particular challenge is the generation of "free chlorine" species such as Cl_2 or HClO which pose issues of safety and corrosion on the anode.[46] While replacing OER or the chloride oxidation reaction with GEOR on a one-to-one molecular basis provides practical challenges of its own, we explored the technical possibility of improving operating cell potential for H_2 evolution from seawater.

Figure 3c shows the *j-E* characteristics of hydrogen evolution from a Pt-Ni foam cathode as measured in simulated seawater (sHER). A load-line analysis predicted operating cell potentials of V_{op} = -0.35 V + V_{BPM} = -1.18 V for a sHER|BPM|GEOR cell and V_{op} = -1.41 V + V_{BPM} = -2.24 V for a sHER|BPM|OER cell at an operating geometric current density of -10.0 mA cm^{-2}. The measured operating cell potentials at -10.0 mA cm^{-2} were -1.55 V for the sHER|BPM|GEOR cell and -2.45 V for the sHER|BPM|OER cell (Figure 3d). The excess potential again is likely related to membrane and solution resistance unaccounted for in the load-line analysis, in addition to the slow oxidation of the anode surface in the case of the GEOR reaction. The cell potential increased by less than 0.1 V in the 20 h period of each experiment. The advantage of using the GEOR anode is evident in the steady 0.9 V reduction in overall cell potential.

We observed a significant acidification of the catholyte in each seawater electrolysis experiment. The pH of the seawater catholyte decreased from an initial value of 8.5 to 1.6 after 20 h of HER. Additionally, we observed the deposition of material on the cathode after 20 h. EDX elemental analysis of the deposited material showed that it mainly consisted of magnesium and oxygen in addition to trace amounts of calcium, sodium, potassium, sulfur, and chlorine (Figure S2 and Table S3). These are all components of the model seawater electrolyte. We hypothesize that the constant formation of OH^- during hydrogen evolution at the cathode forms an alkaline diffusion layer that causes a layer of $Mg(OH)_2$ precipitate to form on the electrode. The deposited layer is stabilized by a diffusion layer formed at the electrode surface, which traps hydroxide from neutralizing the hydronium entering the catholyte as the cation from the BPM. The $Mg(OH)_2$ layer dissolved from the electrode surface and the pH of the acidified seawater catholyte recovered to 8.5 when the electrode was left in it over a 48-hour period without electrolysis. This layer formation been previously observed and strategies for avoiding these depositions have been studied elsewhere.[47–49] The anolyte pH was unaffected by the electrocatalysis and was measured to be 14.2 before and after all reactions regardless of duration of the experiment.

The electrochemical CO_2 reduction reaction (CO_2RR) is ideally a route to close the atmospheric CO_2 cycle by utilizing fossil fuel emissions. The technical goal is the electrochemical conversion of carbon dioxide to fuels (such as CH_4, CH_3OH, C_2H_6),[50–53] hydrogen storage (such as HCOOH),[54–57] or precursors for further utilization (such as CO or C_2H_4).[58–60] CO_2RR is most generally performed in a bicarbonate buffer to maximize CO_2 solubility and to mitigate water reduction.[61] However the buffer limits the kinetics of the OER reaction on the anode. Glycerol has been used to reduce the overall cell potential for CO_2RR in alkaline electrolysis systems.[62] BPMs have been used in CO_2RR to stimulate local HCO_3^--to-CO_2 conversion near the cathode in zero-gap electrolytic systems[35,63,64] and to decouple the anolyte from the catholyte in an photoelectrochemical CO_2RR integrated system.[65] CO_2RR and GEOR have been combined to reduce cell potentials for sustained CO_2 electrolysis at high current densities ($E_{cell} \approx 3.9$ V at 175 mA cm^{-2} on an Au electrocatalyst) in a flow reactor.[66] To our knowledge, the sustained pairing of CO_2RR and GEOR have not been characterized at the low cell potentials of interest to PEC integrated systems, for example.

Figure 3e shows the three-electrode *j-E* characteristics of a Pt-coated Ni foam OER anode in a 0.500 M Na_2CO_3 buffer solution (bOER; pH = 6.8) for comparison to the same anode in a 2.0 M NaOH electrolyte. The more positive potentials required to pass the same anodic current in the Na_2CO_3 buffer can be attributed to the negative Nernstian shift of 0.44 V (= 0.0592 V x ΔpH) of the OER potential at the different pH values. The advantage of OER in the buffered electrolyte is that a Selemion anion exchange membrane can be used rather than a BPM without the need to include a V_{BPM} contribution to the cell potential. We considered each of these anodic half-reactions in a pairing with an Au-coated Ni-foam CO_2RR cathode in a 0.500 M Na_2CO_3 buffer solution. The three-electrode *j-E* characteristic of this cathode is also shown in Figure 3e.

The Au on Ni foam and Au-Pt-Bi-coated electrodes that were used for CO_2RR|BPM|GEOR were compared to as-prepared samples using EDX. We observed a loss of intensity in the EDX features Au-Pt-Bi electrodes show a corresponding to these elements after 24 h of GEOR electrocatalysis (Figure S3a). This loss of electrocatalytic material is likely a factor in cell potential increase over time. Au was present in similar quantities before and after the 24 h CO_2RR, on the Au-coated Ni foam electrocatalyst as seen in Figure S3b. This was expected as metallic Au is thermodynamically stable in the reductive conditions of cathodic operation.[67] Load-line analyses predicted that the operating cell potentials at -10.0 mA cm^{-2} cathodic current were V_{op} = -2.10 V for a CO_2RR|selemion|bOER electrolysis cell, V_{op} = -1.73 V + V_{BPM} = -2.56

V for a CO_2RR|BPM|OER electrolysis cell, and V_{op} = -0.67 V + V_{BPM} = -1.50 V for a CO_2RR|BPM|GEOR electrolysis cell. The measured operating cell potentials for > 15 h CP electrolysis experiments are shown in Figure 3f. The GEOR-assisted cell maintained a steady operating potential of -1.7 V, which is slightly higher than predicted by the LLA, though this was still roughly 1V lower than the cell when the anode side performed OER. Product analysis for the CO_2RR showed that CO and H_2 were the main cathodic products in all cases, independent of the anode reaction. Faradaic efficiencies for products during these CO_2RR experiments are shown in Table S2. Additionally, no change in the pH of the catholyte was observed over the entire reaction, as would be expected from a buffered electrolyte.

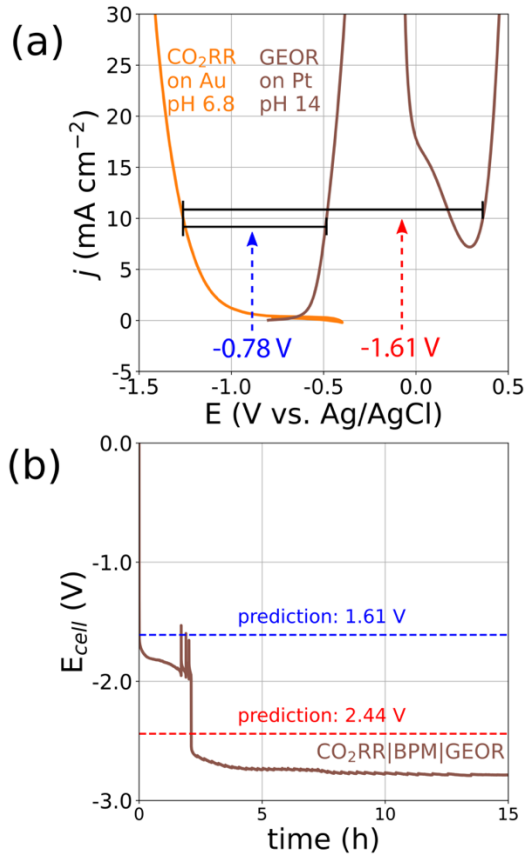

Figure 4 - (a) LLA and (b) chronopotentiometry of HER on Pt-coated Ni in H_2SO_4 paired with GEOR on Pt oxides in 2 M NaOH and glycerol separated by a bipolar membrane. The abrupt cell potential increase and the fluctuation prior are due to Pt oxidation at the anode surface. The blue line represents the prediction of glycerol oxidation on a metallic Pt-coated anode (V_{op} = -0.78 V + V_{BPM} = -1.61V). The red line represents the prediction for GEOR on a platinum oxide-coated anode (V_{op} =-1.61+V_{BPM} = -2.44 V).

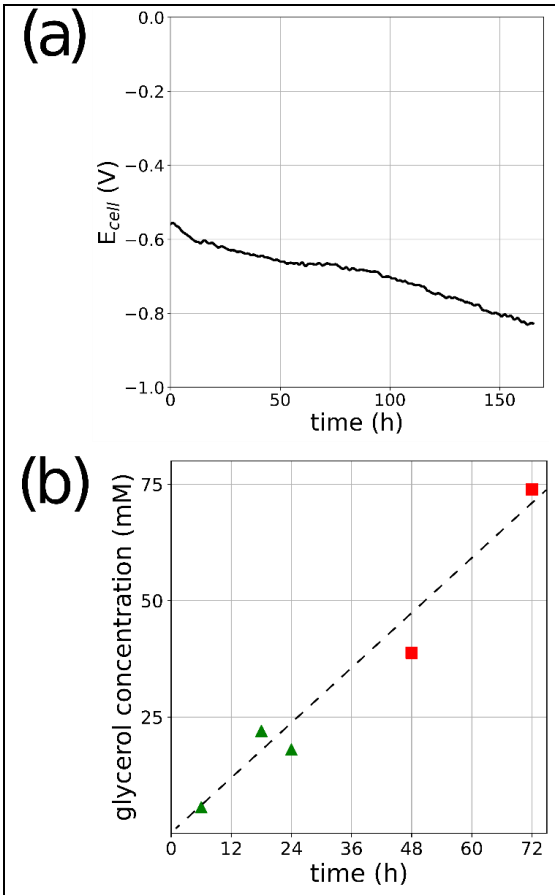

Figure 5: (a) aHER|BPM|GEOR electrocatalyst longevity experiment. Chronopotentiometry at -10.0 mA cm^{-2} for 160 hours. The initial cell potential started was -0.56 V and increased to -0.82 V by the end of the 160 h experiment. (b) Crossover glycerol concentration based on ^{1}H NMR data. Green triangles represent samples collected during the CO_2RR|BPM|GEOR CP experiment at -10mA cm^{-2}. Red squares represent the glycerol crossover concentration after the end of the CP experiment.

As shown in previous work, Pt is nominally the functional electrocatalyst that facilitates the observed low operating cell potentials when assisted by GEOR. Pt can carry out this reaction alone, but not for long durations. The electrochemical oxidation of the Pt interface was observed in the OER *j-E* CV data in Figure 2. Figure 4a shows a LLA for pairing a Pt anode for GEOR with a cathode performing CO_2RR on a Au cathode. Figure 4b shows a CP measurement of a Pt-coated Ni foam anode, which can sustain -10.0 mA cm^{-2} during GEOR in the alkaline conditions used for these experiments. However, after 2.5 h, we observed an abrupt increase in the cell potential, indicating the oxidation of the Pt interface as observed elsewhere.[68] While GEOR may continue at the oxidized Pt interface, it occurs at a more positive absolute potential than on the metallic Pt electrocatalyst. This demonstrates the important role that the additional metals (Au and Bi) play in the durability of the multi-metal electrocatalyst used here for GEOR.

A durability test was performed to determine the effects of degradation of the Au-Pt-Bi electrocatalyst and BPM on the cell potential over an extended period. The two-electrode chronopotentiometry at –10.0 mA cm^{-2} in an aHER|BPM|GEOR cell showed that the cell potentials began at -0.55 V, and remained under -0.7

V for more than 80 h (Figure 5a). The cell potential increased by 267 mV over the 160 h experiment. Prior experiments suggest that bismuth dissolution from the Au-Pt-Bi electrode impacts the GEOR by steadily causing the formation of Pt oxide/hydroxide. Periodic bismuth redeposition (via a quick cathodic pulse on the anode in the presence of Bi^{3+} in the solution) has been shown to be an effective measure to enhance the lifetime of Au-Pt-Bi anode.[27]

NMR measurements of the cathodic chamber electrolyte showed the presence of glycerol in the solution after 6 hours of electrolysis. Over a 24-hour period of electrolysis the concentration of glycerol in 25 mL of catholyte increased to 18 mM. After the CP experiment, the electrolytes were left in the cell for 48 hours to determine if the electrolysis was driving glycerol crossover. The concentration of glycerol in the cathodic chamber after 48 and 72 hours from the beginning of the experiment were 39 mM and 72 mM, respectively. Glycerol permeates through the BPM regardless of whether electrolysis was occurring. The NMR spectra used to quantify glycerol crossover are shown in Figure S6. The permeation rate of glycerol through the BPM was relatively constant in time and calculated to be 6.7 ± 0.4 μmol cm^{-2} h^{-1} from the slope of the NMR-determined concentrations shown in Figure 5b. The effects of this loss of glycerol on the cell potential over the duration of the experiments are small compared to the electrocatalytic consumption of glycerol by anode.

This work shows that a bipolar membrane can be used jointly with a glycerol electrooxidation half-reaction to significantly reduce the overall cell potential for cathodic fuel-forming reactions under conditions independent of the GEOR half-cell. The BPM enables the pairing of an independently optimized cathode (or photocathode) for the reaction of interest while benefiting from the sustained voltage savings resulting from using the GEOR anode described here. Given the relatively low current densities, these results will be most beneficial in the context of PEC-integrated systems rather than high current density electrolysis. For example, sustained -10.0 mA cm^{-2} for HER is a practical goal for a PEC system. Glycerol-assisted HER is possible at less than 0.7 V overall cell potential at that current density for extended periods. This is readily achievable with many single-junction light absorbers, including CdTe or perovskite-based PV.[69,70] Additionally, > 20 h of electrolysis stability suggests that the electrocatalyst layers can be used over the course of a day and then regenerated overnight by electrochemical methods. Reducing the overall cell potential required to generate hydrogen simplifies the design of a PEC system and can leave a portion of the visible solar spectrum unabsorbed for other uses. If a semi-transparent methylammonium lead iodide perovskite solar cell (band gap ≈ 1.7-1.8 eV) is used to

drive glycerol-assisted solar-to-H_2, the transmitted solar illumination could be collected in a Si bottom cell to generate electricity and enhance the efficiency of the process. The efficiency gains of the electrochemical/electrical processes rely on the constant consumption of glycerol as a fuel. This is not practical in general. However, coordinating PEC-based photoelectrolysis with biodiesel production could be practical and may improve the economic prospects of both technologies.

Conclusion

We have shown that the use of GEOR in conjunction with a bipolar membrane can effectively replace OER as an anodic reaction in a variety of electrolysis cells, even those with significantly different electrochemical environments. GEOR can be paired with HER, both in concentrated acid solutions and seawater, and with CO_2RR in bicarbonate buffered solution. We showed that a load-line analysis can be used as a method for predicting the overall cell potential in a two-electrode electrochemical setup. The overall cell potential of the GEOR-BPM electrochemical cell paired with HER and CO_2RR was 1 V less that of a conventional OER-membrane cell at -10.0 mA cm^{-2}. The Au-Pt-Bi-coated Ni foam electrocatalyst was shown to be stable for greater than 20 h periods at -10.0 mA cm^{-2} during GEOR. Minimal glycerol migration through the BPM was observed. This device design may help to facilitate PEC solar fuels systems that rely on alternative oxidation reactions.

Supporting Information Available

Description of the relevant electrochemical reactions for load line analysis, reactor geometry, and analytical measurements.

Acknowledgement

This material is based upon work supported by the U.S. Department of Energy, Office of Science, Office of Basic Energy Sciences under Award Number DE-SC-0020301.

References

(1) Kumar, B.; Llorente, M.; Froehlich, J.; Dang, T.; Sathrum, A.; Kubiak, C. P. Photochemical and Photoelectrochemical Reduction of CO_2. *Annu. Rev. Phys. Chem.* **2012**, *63* (1), 541–569. https://doi.org/10.1146/annurev-physchem-032511-143759.

(2) Xiang, C.; Weber, A.; Ardo, S.; Berger, A.; Chen, Y.; Coridan, R.; Fountaine, K.; Haussener, S.; Hu, S.; Liu, R.; Lewis, N.; Modestino, M.; Shaner, M.; Singh, M.; Stevens, J.; Sun, K.; Walczak, K. Modeling, Simulation, and Implementation of Solar-Driven Water-Splitting Devices. *Angew. Chem.-Int. Ed.* **2016**, *55* (42), 12974–12988. https://doi.org/10.1002/anie.201510463.

(3) Cheng, W.; Richter, M.; May, M.; Ohlmann, J.; Lackner, D.; Dimroth, F.; Hannappel, T.; Atwater, H.; Lewerenz, H. Monolithic Photoelectrochemical Device for Direct Water Splitting with 19% Efficiency. *ACS ENERGY Lett.* **2018**, *3* (8), 1795–1800. https://doi.org/10.1021/acsenergylett.8b00920.

(4) Conibeer, G. J.; Richards, B. S. A Comparison of PV/Electrolyser and Photoelectrolytic Technologies for Use in Solar to Hydrogen Energy Storage Systems. *Int. J. Hydrog. Energy* **2007**, *32* (14), 2703–2711. https://doi.org/10.1016/j.ijhydene.2006.09.012.

(5) Fan, S.; AlOtaibi, B.; Woo, S. Y.; Wang, Y.; Botton, G. A.; Mi, Z. High Efficiency Solar-to-Hydrogen Conversion on a Monolithically Integrated InGaN/GaN/Si Adaptive Tunnel Junction Photocathode. *Nano Lett.* **2015**, *15* (4), 2721–2726. https://doi.org/10.1021/acs.nanolett.5b00535.

(6) May, M. M.; Lewerenz, H.-J.; Lackner, D.; Dimroth, F.; Hannappel, T. Efficient Direct Solar-to-Hydrogen Conversion by in Situ Interface Transformation of a Tandem Structure. *Nat. Commun.* **2015**, *6* (1), 8286. https://doi.org/10.1038/ncomms9286.

(7) Ahn, S. T.; Abu-Baker, I.; Palmore, G. T. R. Electroreduction of CO_2 on Polycrystalline Copper: Effect of Temperature on Product Selectivity. *Catal. Today* **2017**, *288*, 24–29. https://doi.org/10.1016/j.cattod.2016.09.028.

(8) Barton, E. E.; Rampulla, D. M.; Bocarsly, A. B. Selective Solar-Driven Reduction of CO2 to Methanol Using a Catalyzed p-GaP Based Photoelectrochemical Cell. *J. Am. Chem. Soc.* **2008**, *130* (20), 6342–6344. https://doi.org/10.1021/ja0776327.

(9) Ji, G.; Liu, Y.; Zhu, L.; Wang, J.; Zhang, B.; Chang, X.; Gondal, M.; Dastageer, M. A. High-Active Direct Z-Scheme Si/TiO2 Photocatalyst for Boosted CO2 Reduction into Value-Added Methanol. *RSC Adv.* **2014**. https://doi.org/10.1039/C4RA10670A.

(10) Matsuoka, K.; Inaba, M.; Iriyama, Y.; Abe, T.; Ogumi, Z.; Matsuoka, M. Anodic Oxidation of Polyhydric Alcohols on a Pt Electrode in Alkaline Solution. *FUEL CELLS* **2002**, *2* (1), 35–39. https://doi.org/10.1002/1615-6854(20020815)2:1<35::AID-FUCE35>3.0.CO;2-2.

(11) Ge, X.; Wang, R.; Liu, P.; Ding, Y. Platinum-Decorated Nanoporous Gold Leaf for Methanol Electrooxidation. *Chem. Mater.* **2007**, *19* (24), 5827–5829. https://doi.org/10.1021/cm702335f.

(12) Ferrin, P.; Mavrikakis, M. Structure Sensitivity of Methanol Electrooxidation on Transition Metals. *J. Am. Chem. Soc.* **2009**, *131* (40), 14381–14389. https://doi.org/10.1021/ja904010u.

(13) Sun, F.; Qin, J.; Wang, Z.; Yu, M.; Wu, X.; Sun, X.; Qiu, J. Energy-Saving Hydrogen Production by Chlorine-Free Hybrid Seawater Splitting Coupling Hydrazine Degradation. *Nat. Commun.* **2021**, *12* (1), 4182. https://doi.org/10.1038/s41467-021-24529-3.

(14) Simoes, M.; Baranton, S.; Coutanceau, C. Electrochemical Valorisation of Glycerol. *CHEMSUSCHEM* **2012**, *5* (11), 2106–2124. https://doi.org/10.1002/cssc.201200335.

(15) Zalineeva, A.; Serov, A.; Padilla, M.; Martinez, U.; Artyushkova, K.; Baranton, S.; Coutanceau, C.; Atanassov, P. B. Glycerol Electrooxidation on Self-Supported Pd1Snx Nanoparticules. *Appl. Catal. B Environ.* **2015**, *176–177*, 429–435. https://doi.org/10.1016/j.apcatb.2015.04.037.

(16) Mello, G.; Buso-Rogero, C.; Herrero, E.; Feliu, J. Glycerol Electrooxidation on Pd Modified Au Surfaces in Alkaline Media: Effect of the Deposition Method. *J. Chem. Phys.* **2019**, *150* (4). https://doi.org/10.1063/1.5048489.
(17) de Souza, M. B. C.; Vicente, R. A.; Yukuhiro, V. Y.; V. M. T. Pires, C. T. G.; Cheuquepán, W.; Bott-Neto, J. L.; Solla-Gullón, J.; Fernández, P. S. Bi-Modified Pt Electrodes toward Glycerol Electrooxidation in Alkaline Solution: Effects on Activity and Selectivity. *ACS Catal.* **2019**, *9* (6), 5104–5110. https://doi.org/10.1021/acscatal.9b00190.
(18) Hu, S.; Luo, X.; Wan, C.; Li, Y. Characterization of Crude Glycerol from Biodiesel Plants. *J. Agric. FOOD Chem.* **2012**, *60* (23), 5915–5921. https://doi.org/10.1021/jf3008629.
(19) Yang, F.; Hanna, M.; Sun, R. Value-Added Uses for Crude Glycerol-a Byproduct of Biodiesel Production. *Biotechnol. BIOFUELS* **2012**, *5*. https://doi.org/10.1186/1754-6834-5-13.
(20) Bagheri, S.; Julkapli, N.; Yehye, W. Catalytic Conversion of Biodiesel Derived Raw Glycerol to Value Added Products. *Renew. Sustain. ENERGY Rev.* **2015**, *41*, 113–127. https://doi.org/10.1016/j.rser.2014.08.031.
(21) Qureshi, F.; Yusuf, M.; Pasha, A. A.; Khan, H. W.; Imteyaz, B.; Irshad, K. Sustainable and Energy Efficient Hydrogen Production via Glycerol Reforming Techniques: A Review. *Int. J. Hydrog. Energy* **2022**, *47* (98), 41397–41420. https://doi.org/10.1016/j.ijhydene.2022.04.010.
(22) Villa, A.; Veith, G. M.; Prati, L. Selective Oxidation of Glycerol under Acidic Conditions Using Gold Catalysts. *Angew. Chem. Int. Ed.* **2010**, *49* (26), 4499–4502. https://doi.org/10.1002/anie.201000762.
(23) Oliveira, V.; Morais, C.; Servat, K.; Napporn, T.; Tremiliosi-Filho, G.; Kokoh, K. Glycerol Oxidation on Nickel Based Nanocatalysts in Alkaline Medium - Identification of the Reaction Products. *J. Electroanal. Chem.* **2013**, *703*, 56–62. https://doi.org/10.1016/j.jelechem.2013.05.021.
(24) Valter, M.; Busch, M.; Wickman, B.; Grönbeck, H.; Baltrusaitis, J.; Hellman, A. Electrooxidation of Glycerol on Gold in Acidic Medium: A Combined Experimental and DFT Study. *J. Phys. Chem. C* **2018**, *122* (19), 10489–10494. https://doi.org/10.1021/acs.jpcc.8b02685.
(25) Da Silva, R.; Neto, S.; Kokoh, K.; De Andrade, A. Electroconversion of Glycerol in Alkaline Medium: From Generation of Energy to Formation of Value-Added Products. *J. POWER SOURCES* **2017**, *351*, 174–182. https://doi.org/10.1016/j.jpowsour.2017.03.101.
(26) Dodekatos, G.; Schünemann, S.; Tüysüz, H. Recent Advances in Thermo-, Photo-, and Electrocatalytic Glycerol Oxidation. *ACS Catal.* **2018**, *8* (7), 6301–6333. https://doi.org/10.1021/acscatal.8b01317.
(27) Schichtl, Z. G.; Conlin, S. K.; Mehrabi, H.; Nielander, A. C.; Coridan, R. H. Characterizing Sustained Solar-to-Hydrogen Electrocatalysis at Low Cell Potentials Enabled by Crude Glycerol Oxidation. *ACS Appl. Energy Mater.* **2022**, *5* (3), 3863–3875. https://doi.org/10.1021/acsaem.2c00377.
(28) Lobyntseva, E.; Kallio, T.; Kontturi, K. Bipolar Membranes in Forward Bias Region for Fuel Cell Reactors. *Electrochimica Acta* **2006**, *51* (7), 1165–1171. https://doi.org/10.1016/j.electacta.2005.06.004.
(29) Giesbrecht, P. K.; Freund, M. S. Recent Advances in Bipolar Membrane Design and Applications. *Chem. Mater.* **2020**, *32* (19), 8060–8090. https://doi.org/10.1021/acs.chemmater.0c02829.
(30) Chen, L.; Xu, Q.; Oener, S. Z.; Fabrizio, K.; Boettcher, S. W. Design Principles for Water Dissociation Catalysts in High-Performance Bipolar Membranes. *Nat. Commun.* **2022**, *13* (1), 3846. https://doi.org/10.1038/s41467-022-31429-7.
(31) Oener, S. Z.; Foster, M. J.; Boettcher, S. W. Accelerating Water Dissociation in Bipolar Membranes and for Electrocatalysis. *Science* **2020**, *369* (6507), 1099–1103. https://doi.org/10.1126/science.aaz1487.

(32) Mafé, S.; Ramírez, P.; Alcaraz, A. Electric Field-Assisted Proton Transfer and Water Dissociation at the Junction of a Fixed-Charge Bipolar Membrane. *Chem. Phys. Lett.* **1998**, *294* (4), 406–412. https://doi.org/10.1016/S0009-2614(98)00877-X.
(33) Oener, S. Z.; Twight, L. P.; Lindquist, G. A.; Boettcher, S. W. Thin Cation-Exchange Layers Enable High-Current-Density Bipolar Membrane Electrolyzers via Improved Water Transport. *ACS Energy Lett.* **2021**, *6* (1), 1–8. https://doi.org/10.1021/acsenergylett.0c02078.
(34) McDonald, M. B.; Ardo, S.; Lewis, N. S.; Freund, M. S. Use of Bipolar Membranes for Maintaining Steady-State PH Gradients in Membrane-Supported, Solar-Driven Water Splitting. *ChemSusChem* **2014**, *7* (11), 3021–3027. https://doi.org/10.1002/cssc.201402288.
(35) Li, Y. C.; Zhou, D.; Yan, Z.; Gonçalves, R. H.; Salvatore, D. A.; Berlinguette, C. P.; Mallouk, T. E. Electrolysis of CO2 to Syngas in Bipolar Membrane-Based Electrochemical Cells. *ACS Energy Lett.* **2016**, *1* (6), 1149–1153. https://doi.org/10.1021/acsenergylett.6b00475.
(36) Chabi, S.; Wright, A. G.; Holdcroft, S.; Freund, M. S. Transparent Bipolar Membrane for Water Splitting Applications. *ACS Appl. Mater. Interfaces* **2017**, *9* (32), 26749–26755. https://doi.org/10.1021/acsami.7b04402.
(37) Coridan, R. H.; Nielander, A. C.; Francis, S. A.; McDowell, M. T.; Dix, V.; Chatman, S. M.; Lewis, N. S. Methods for Comparing the Performance of Energy-Conversion Systems for Use in Solar Fuels and Solar Electricity Generation. *Energy Environ. Sci.* **2015**, *8* (10), 2886–2901. https://doi.org/10.1039/C5EE00777A.
(38) Chu, S.; Li, W.; Yan, Y.; Hamann, T.; Shih, I.; Wang, D.; Mi, Z. Roadmap on Solar Water Splitting: Current Status and Future Prospects. *Nano Futur.* **2017**, *1* (2), 022001. https://doi.org/10.1088/2399-1984/aa88a1.
(39) Bard, A. J.; Faulkner, L. R. *Electrochemical Methods: Fundamentals and Applications*, 2nd ed.; Wiley: New York, 2001.
(40) Luo, J.; Vermaas, D. A.; Bi, D.; Hagfeldt, A.; Smith, W. A.; Grätzel, M. Bipolar Membrane-Assisted Solar Water Splitting in Optimal PH. *Adv. Energy Mater.* **2016**, *6* (13), 1600100. https://doi.org/10.1002/aenm.201600100.
(41) McDonald, M. B.; Bruce, J. P.; McEleney, K.; Freund, M. S. Reduced Graphene Oxide Bipolar Membranes for Integrated Solar Water Splitting in Optimal PH. *ChemSusChem* **2015**, *8* (16), 2645–2654. https://doi.org/10.1002/cssc.201500538.
(42) Blommaert, M. A.; Aili, D.; Tufa, R. A.; Li, Q.; Smith, W. A.; Vermaas, D. A. Insights and Challenges for Applying Bipolar Membranes in Advanced Electrochemical Energy Systems. *ACS Energy Lett.* **2021**, *6* (7), 2539–2548. https://doi.org/10.1021/acsenergylett.1c00618.
(43) Chen, Y.; Wrubel, J. A.; Klein, W. E.; Kabir, S.; Smith, W. A.; Neyerlin, K. C.; Deutsch, T. G. High-Performance Bipolar Membrane Development for Improved Water Dissociation. *ACS Appl. Polym. Mater.* **2020**, *2* (11), 4559–4569. https://doi.org/10.1021/acsapm.0c00653.
(44) Wrubel, J. A.; Chen, Y.; Ma, Z.; Deutsch, T. G. Modeling Water Electrolysis in Bipolar Membranes. *J. Electrochem. Soc.* **2020**, *167* (11), 114502. https://doi.org/10.1149/1945-7111/ab9ccb.
(45) Bolar, S.; Shit, S.; Murmu, N. C.; Kuila, T. Progress in Theoretical and Experimental Investigation on Seawater Electrolysis: Opportunities and Challenges. *Sustain. Energy Fuels* **2021**, *5* (23), 5915–5945. https://doi.org/10.1039/D1SE01347E.
(46) Marin, D. H.; Perryman, J. T.; Hubert, M. A.; Lindquist, G. A.; Chen, L.; Aleman, A. M.; Kamat, G. A.; Niemann, V. A.; Stevens, M. B.; Regmi, Y. N.; Boettcher, S. W.; Nielander, A. C.; Jaramillo, T. F. Hydrogen Production with Seawater-Resilient Bipolar Membrane Electrolyzers. *Joule* **2023**, *7* (4), 765–781. https://doi.org/10.1016/j.joule.2023.03.005.
(47) Dresp, S.; Dionigi, F.; Klingenhof, M.; Strasser, P. Direct Electrolytic Splitting of Seawater: Opportunities and Challenges. *ACS Energy Lett.* **2019**, *4* (4), 933–942. https://doi.org/10.1021/acsenergylett.9b00220.

(48) Mohammed-Ibrahim, J.; Moussab, H. Recent Advances on Hydrogen Production through Seawater Electrolysis. *Mater. Sci. Energy Technol.* **2020**, *3*, 780–807. https://doi.org/10.1016/j.mset.2020.09.005.
(49) Guo, J.; Zheng, Y.; Hu, Z.; Zheng, C.; Mao, J.; Du, K.; Jaroniec, M.; Qiao, S.-Z.; Ling, T. Direct Seawater Electrolysis by Adjusting the Local Reaction Environment of a Catalyst. *Nat. Energy* **2023**, 1–9. https://doi.org/10.1038/s41560-023-01195-x.
(50) Cook, R. L.; MacDuff, R. C.; Sammells, A. F. High Rate Gas Phase CO 2 Reduction to Ethylene and Methane Using Gas Diffusion Electrodes. *J. Electrochem. Soc.* **1990**, *137* (2), 607–608.
(51) Kuhl, K. P.; Cave, E. R.; Abram, D. N.; Jaramillo, T. F. New Insights into the Electrochemical Reduction of Carbon Dioxide on Metallic Copper Surfaces. *Energy Environ. Sci.* **2012**, *5* (5), 7050. https://doi.org/10.1039/c2ee21234j.
(52) Kuhl, K. P.; Hatsukade, T.; Cave, E. R.; Abram, D. N.; Kibsgaard, J.; Jaramillo, T. F. Electrocatalytic Conversion of Carbon Dioxide to Methane and Methanol on Transition Metal Surfaces. *J. Am. Chem. Soc.* **2014**, *136* (40), 14107–14113. https://doi.org/10.1021/ja505791r.
(53) Mehrabi, H.; Conlin, S. K.; Hollis, T. I.; Gattis, B. S.; Nelson Weker, J.; Coridan, R. H. Electrochemical Control of the Morphology and Functional Properties of Hierarchically Structured, Dendritic Cu Surfaces. *Energy Technol.* **2023**, *11* (3), 2201124. https://doi.org/10.1002/ente.202201124.
(54) Zaidman, B.; Wiener, H.; Sasson, Y. Formate Salts as Chemical Carriers in Hydrogen Storage and Transportation. *Int. J. Hydrog. Energy* **1986**, *11* (5), 341–347. https://doi.org/10.1016/0360-3199(86)90154-0.
(55) Boddien, A.; Junge, H. Acidic Ideas for Hydrogen Storage. *Nat. Nanotechnol.* **2011**, *6* (5), 265–266. https://doi.org/10.1038/nnano.2011.70.
(56) Boddien, A.; Gärtner, F.; Federsel, C.; Sponholz, P.; Mellmann, D.; Jackstell, R.; Junge, H.; Beller, M. CO2-"Neutral" Hydrogen Storage Based on Bicarbonates and Formates. *Angew. Chem. Int. Ed.* **2011**, *50* (28), 6411–6414. https://doi.org/10.1002/anie.201101995.
(57) Russo, D.; Calabrese, M.; Marotta, R.; Andreozzi, R.; Di Benedetto, A. Thermodynamics of the Cyclic Formate/Bicarbonate Interconversion for Hydrogen Storage. *Int. J. Hydrog. Energy* **2022**, *47* (73), 31370–31380. https://doi.org/10.1016/j.ijhydene.2022.07.033.
(58) Li, J.; Chang, K.; Zhang, H.; He, M.; Goddard, W. A.; Chen, J. G.; Cheng, M.-J.; Lu, Q. Effectively Increased Efficiency for Electroreduction of Carbon Monoxide Using Supported Polycrystalline Copper Powder Electrocatalysts. *Acs Catal.* **2019**, *9* (6), 4709–4718. https://doi.org/10.1021/acscatal.9b00099.
(59) Gao, D.; Sinev, I.; Scholten, F.; Arán-Ais, R. M.; Divins, N. J.; Kvashnina, K.; Timoshenko, J.; Cuenya, B. R. Selective CO2 Electroreduction to Ethylene and Multicarbon Alcohols via Electrolyte-Driven Nanostructuring. *Angew. Chem. Int. Ed.* **2019**, *58* (47), 17047–17053. https://doi.org/10.1002/anie.201910155.
(60) Zhang, W.; Huang, C.; Xiao, Q.; Yu, L.; Shuai, L.; An, P.; Zhang, J.; Qiu, M.; Ren, Z.; Yu, Y. Atypical Oxygen-Bearing Copper Boosts Ethylene Selectivity toward Electrocatalytic CO_2 Reduction. *J. Am. Chem. Soc.* **2020**, *142* (26), 11417–11427. https://doi.org/10.1021/jacs.0c01562.
(61) Goyal, A.; Marcandalli, G.; Mints, V. A.; Koper, M. T. M. Competition between CO2 Reduction and Hydrogen Evolution on a Gold Electrode under Well-Defined Mass Transport Conditions. *J. Am. Chem. Soc.* **2020**, *142* (9), 4154–4161. https://doi.org/10.1021/jacs.9b10061.
(62) Verma, S.; Lu, S.; Kenis, P. J. A. Co-Electrolysis of CO2 and Glycerol as a Pathway to Carbon Chemicals with Improved Technoeconomics Due to Low Electricity Consumption. *Nat. Energy* **2019**, *4* (6), 466–474. https://doi.org/10.1038/s41560-019-0374-6.
(63) Xie, K.; Miao, R. K.; Ozden, A.; Liu, S.; Chen, Z.; Dinh, C.-T.; Huang, J. E.; Xu, Q.; Gabardo, C. M.; Lee, G.; Edwards, J. P.; O'Brien, C. P.; Boettcher, S. W.; Sinton, D.; Sargent, E. H. Bipolar Membrane

Electrolyzers Enable High Single-Pass CO2 Electroreduction to Multicarbon Products. *Nat. Commun.* **2022**, *13* (1), 3609. https://doi.org/10.1038/s41467-022-31295-3.
(64) Siritanaratkul, B.; Forster, M.; Greenwell, F.; Sharma, P. K.; Yu, E. H.; Cowan, A. J. Zero-Gap Bipolar Membrane Electrolyzer for Carbon Dioxide Reduction Using Acid-Tolerant Molecular Electrocatalysts. *J. Am. Chem. Soc.* **2022**, *144* (17), 7551–7556. https://doi.org/10.1021/jacs.1c13024.
(65) Zhou, X.; Liu, R.; Sun, K.; Chen, Y.; Verlage, E.; Francis, S. A.; Lewis, N. S.; Xiang, C. Solar-Driven Reduction of 1 Atm of CO2 to Formate at 10% Energy-Conversion Efficiency by Use of a TiO2-Protected III–V Tandem Photoanode in Conjunction with a Bipolar Membrane and a Pd/C Cathode. *ACS Energy Lett.* **2016**, *1* (4), 764–770. https://doi.org/10.1021/acsenergylett.6b00317.
(66) Khan, M. A.; Nabil, S. K.; Al-Attas, T.; Yasri, N. G.; Roy, S.; Rahman, M. M.; Larter, S.; Ajayan, P. M.; Hu, J.; Kibria, M. G. Zero-Crossover Electrochemical CO2 Reduction to Ethylene with Co-Production of Valuable Chemicals. *Chem Catal.* **2022**, *2* (8), 2077–2095. https://doi.org/10.1016/j.checat.2022.06.018.
(67) Revie, R. W. *Uhlig's Corrosion Handbook*; John Wiley & Sons, 2011.
(68) Schichtl, Z. G.; Mehrabi, H.; Coridan, R. H. Electrooxidation of Glycerol on Self-Organized, Mixed Au–Pt Interfaces Formed on Ni Substrates. *J. Electrochem. Soc.* **2020**, *167* (5), 056502. https://doi.org/10.1149/1945-7111/ab679e.
(69) Zhao, Y.; Boccard, M.; Liu, S.; Becker, J.; Zhao, X.-H.; Campbell, C. M.; Suarez, E.; Lassise, M. B.; Holman, Z.; Zhang, Y.-H. Monocrystalline CdTe Solar Cells with Open-Circuit Voltage over 1 V and Efficiency of 17%. *Nat. Energy* **2016**, *1* (6), 1–7. https://doi.org/10.1038/nenergy.2016.67.
(70) Chen, P.; Bai, Y.; Wang, L. Minimizing Voltage Losses in Perovskite Solar Cells. *Small Struct.* **2021**, *2* (1), 2000050. https://doi.org/10.1002/sstr.202000050.